

1 **Oscillations of the Ionosphere Caused by the 2022**
2 **Tonga Volcanic Eruption Observed with SuperDARN**
3 **Radars**

4 **Jiaojiao Zhang^{1,2}, Jiayao Xu^{1,2}, Wei Wang^{1,2}, Guojun Wang^{1,2}, J. Michael**
5 **Ruohoniemi³, Atsuki Shinbori⁴, Nozomu Nishitani⁴, Chi Wang^{1,2}, Xiang**
6 **Deng¹, Ailan Lan^{1,2}, and Jingye Yan^{1,2}**

7 ¹State Key Laboratory of Space Weather, National Space Science Center, Chinese Academy of Sciences,
8 Beijing, China

9 ²University of Chinese Academy of Sciences, Beijing, China

10 ³Center for Space Science and Engineering Research (Space@VT), Virginia Polytechnic Institute and
11 State University, Blacksburg, VA, USA

12 ⁴Institute for Space-Earth Environmental Research, Nagoya University, Nagoya, Japan

13 **Key Points:**

- 14 • Enhanced ionospheric irregularities with highly variable velocities were observed
15 after the Tonga volcanic eruption.
16 • The maximum amplitude of the line-of-sight velocity of the ionospheric oscillation
17 approached 150 m/s in E layer.
18 • The ionosphere was displaced upward by as much as 100 km.

Corresponding author: Jiaojiao Zhang, jjzhang@spaceweather.ac.cn

Abstract

On 15 January 2022, the submarine volcano on the southwest Pacific island of Tonga violently erupted. Thus far, the ionospheric oscillation features caused by the volcanic eruption have not been identified. Here, observations from the Super Dual Auroral Radar Network (SuperDARN) radars and digisondes were employed to analyze ionospheric oscillations in the Northern Hemisphere caused by the volcanic eruption in Tonga. Due to the magnetic field conjugate effect, the ionospheric oscillations were observed much earlier than the arrival of surface air pressure waves, and the maximum negative line-of-sight (LOS) velocity of the ionospheric oscillations exceeded 100 m/s in the F layer. After the surface air pressure waves arrived, the maximum LOS velocity in the E layer approached 150 m/s. A maximum upward displacement of 100 km was observed in the ionosphere. This work provides a new perspective for understanding the strong ionospheric oscillation caused by geological hazards observed on Earth.

Plain Language Summary

On 15 January 2022, an underwater volcano on the southwest Pacific island of Tonga erupted, triggering significant disturbances on the surface and in the ionosphere that propagated worldwide. The oscillation features of the ionosphere caused by the volcanic eruption have not been identified. The volcanic eruption caused numerous irregularities in the ionosphere. These irregularities move with the ionosphere similar to how leaves move in a rough sea. In this study, the ionospheric irregularities were observed and employed as tracers to analyze the ionospheric oscillations. Different features of ionospheric oscillations, including the maximum line-of-sight (LOS) velocity, the altitude of the maximum LOS velocity, and the propagation direction, were observed before and after the arrival of the surface air pressure waves. The amplitudes of the LOS velocities of the ionospheric fluctuations approached 150 m/s, and a maximum upward displacement of 100 km, which is the strongest ionospheric fluctuation caused by geological hazards ever observed.

1 Introduction

At 04:14:45 UTC on 15 January, 2022, the Hunga Tonga-Hunga Ha'apai submarine volcano (hereafter referred to as the Tonga volcano), which is centered at 20.546°S, 175.390°W, explosively erupted. Immense ripples on the sea surface and in the atmosphere rapidly spread outward. The volcanic explosivity index (VEI) was estimated to be 6, indicating that this eruption was one of the largest volcanic eruptions recorded in the modern era (Poli & Shapiro, 2022). The volcanic eruption released a large amount of material and energy into the atmosphere, with the highest overshooting tops of the volcanic plume reaching the lower mesosphere at an altitude of ~ 55 km according to satellite imagery (Carr et al., 2022). The waves triggered by the Tonga volcanic eruption on the surface and in the ionosphere were observed worldwide by various ground- and space-based instrumentation (Adam, 2022; Wright et al., 2022; X. Liu et al., 2022).

It is well known that volcanic eruptions and earthquakes can produce measurable ionospheric waves that travel thousands of kilometers (Roberts et al., 1982; Meng et al., 2019). Previous studies on ionospheric disturbances caused by volcanic eruptions, earthquakes, or tsunamis mainly involved total electron content (TEC) variations and horizontal phase velocities of the waves (C. H. Liu et al., 1982; Heki, 2006; Dautermann et al., 2009; Huang et al., 2019). Studies on direct observations of the ionospheric oscillation velocity or amplitude caused by these natural hazards are rare (Nishitani et al., 2011). After the Tonga volcanic eruption, the dense Global Navigation Satellite System (GNSS) receiver network was selected to rapidly analyze the TEC perturbations associated with the volcanic eruption. Themens et al. (2022) identified two large-scale traveling ionospher-

ic disturbances (LSTIDs) with initial speeds of 950 m/s and 555 m/s. The two LSTIDs exhibited strong directionality and slowed down substantially with radial distance. Flowing the two LSTIDs, medium-scale TIDs (MSTIDs) with speeds of 200-400 m/s were observed and propagated globally. Zhang et al. (2022) discovered that the radial two-way disturbance propagation along the entire great circle lasted 4 days. This observation showed that the waves travelled around the globe three times as Lamb waves with primary speeds in the range of 300-350 m/s. Lin et al. (2022) observed the simultaneous occurrence of concentric TIDs (CTIDs) in Australia and Japan between 0800 and 1000 universal time (UT) on 15 January 2022. CTIDs observed in Japan were attributed to the magnetic field conjugate effect. The authors explained that the polarization electric field originated from an E-region dynamo driven by atmospheric disturbance waves in the Southern Hemisphere can be transmitted to magnetically conjugate regions in the Northern Hemisphere along conductive geomagnetic field lines with Alfvénic speed (300 km/s), which is much faster than the speed of Lamb waves. The external electric field, which originated from the conjugate hemisphere generated the CTIDs observed in Japan. Shinbori et al. (2022) studied the electromagnetic conjugate effect of ionospheric disturbances after the Tonga volcanic eruption by using observations from the GNSS-TEC and Super Dual Auroral Radar Network (SuperDARN) Hokkaido radars, which further confirmed the explanation by Lin et al. (2022). However, the Tonga volcanic eruption effects on ionospheric oscillations, especially in the vertical direction, have not been well demonstrated.

Field-aligned electron density irregularities are small-scale density structures in the ionospheric plasma. When the ionosphere fluctuates, these structures move with the ionosphere. Thus, ionospheric irregularities are good tracers for ionospheric movement. SuperDARN radars are powerful tools for observing the motion of irregularities in the ionosphere (Chisham et al., 2007; Nishitani et al., 2019). In this study, ionospheric irregularities observed by using mid-latitude SuperDARN radars and digisondes were employed as tracers to study ionospheric oscillation features in the Northern Hemisphere. It is very interesting that there were different ionospheric oscillation features, such as the maximum LOS velocity and the altitude of the maximum LOS velocity, before and after the arrival of the surface air pressure waves, indicating that the mechanisms of ionospheric oscillations were different in the two stages. In particular, the observations also revealed a significant vertical oscillation of the ionosphere caused by the volcanic eruption.

2 Data

SuperDARN is a global high frequency (HF), coherent scatter radar network that consists of more than 30 radars that observe Earth's upper atmosphere beginning at mid-latitudes and extending to polar regions in both hemispheres. There are now 37 SuperDARN radars, with 22 radars located in high-latitude and polar regions and 15 radars located in mid-latitude regions. The SuperDARN radars are sensitive to Bragg scattering from field-aligned electron density irregularities in the ionosphere (Greenwald et al., 1995). These radars operate in the HF band of the radio spectrum between 8 and 20 MHz; at these frequencies, radar signals are refracted by the ionosphere. The signals return to the radar along the same path, with the incident radar signal orthogonal to the magnetic field. The scale size of the irregularities from which the signal is scattered is equal to one-half of the radar wavelength. The HF signals are refracted toward the ground, and part of the signal may be reflected to the radar. Therefore, in addition to the backscatter received from ionospheric irregularities, SuperDARN radars receive backscatter from the ground or sea surface. The transmission of a multipulse scheme is used to calculate autocorrelation functions (ACFs) of the backscattered signals as a function of range. In each range gate, the ACF is analyzed by a fitting routine known as FITACF that estimates the backscatter power, the LOS Doppler velocity of the irregularities and the spectral width (Ribeiro et al., 2013). A typical SuperDARN radar monitors 16 or 24 beam

120 directions separated by 3.24 degrees in the azimuthal direction, with the 75 ~ 100 range
 121 gates along each beam separated by 45 km. The dwell time of each beam is typically 2 ~
 122 7 s (integration period), which produces a 1 ~ 2 min azimuthal scan.

123 The high-latitude SuperDARN radars are mainly employed to research the iono-
 124 spheric convection driven by solar wind and magnetospheric interactions. Compared with
 125 radars located in high latitudes, mid-latitude radars are more suitable for research on
 126 sub-auroral phenomena and ion-neutral interactions, for example, TIDs. During the vol-
 127 canic eruption in Tonga, data from four mid-latitude SuperDARN radars were available.
 128 These radars included the Jiamusi radar (JME) in China (geographic coordinates of 46.816°N,
 129 130.402°E), the Hokkaido East radar (HOK) (geographic coordinates of 43.53°N, 143.61°E),
 130 the Hokkaido West radar (HKW) in Japan (geographic coordinates of 43.54°N, 143.61°E),
 131 and the Blackstone radar (BKS) in the United States (geographic coordinates of 37.10°N,
 132 77.95°W). Observations from these four radars were used to analyze the ionospheric os-
 133 cillations in this study. The fields of view (FOVs) of the four radars are shown in Fig-
 134 ure 1, where beam 0 of the JME radar and beam 4 of the HOK, HKW and BKS radars
 135 are shown in blue. Beam 0 is the east-most beam of these four radars. The JME and
 136 BKS radars have 24 beams, while the HOK and HKW radars have 16 beams. On 15 Jan-
 137 uary 2022, all four radars were operating in normal (fast) mode, and sequentially sam-
 138 pled beams with a 2-3 s integration time for each beam; thus, the whole FOV was sam-
 139 pled every minute. The operating frequencies of the HOK, HKW and JME radars on
 140 15 January 2022 were 11.07 MHz, 10.08 MHz, and 10.4 MHz, respectively. The operat-
 141 ing frequency of the BKS radar was 10.8 MHz before 1300 UT and 11.5 MHz after 1300
 142 UT.

143 The SuperDARN radars are used to observe the LOS velocities of plasma. In ad-
 144 dition to the SuperDARN radar data, ionogram data from two digisondes located in Mo-
 145 he, Heilongjiang, China (geographic coordinates of 52.0° N, 122.52° E) and Boulder, Col-
 146 orado, USA (geographic coordinates of 40.0°N, 105.3°W) were used to investigate the
 147 height variations in the ionosphere. The densities and heights of the peaks of layers E,
 148 Es, F1, and F2 and electron density profiles up to 1000 km can be automatically calcu-
 149 lated by digisondes. The Mohe ionogram data were obtained from the Chinese Meridi-
 150 an Project Database, and the Boulder ionogram data were obtained from the Digital
 151 Ionogram Database (Reinisch & Galkin, 2011).

152 3 Results

153 3.1 LOS velocity observed by the four SuperDARN radars

154 Range-time-intensity (RTI) plots of the LOS Doppler velocities observed by (a) beam
 155 4 of the HOK radar, (b) beam 0 of the JME radar, (c) beam 4 of the HKW radar and
 156 (d) beam 4 of the BKS radar on 15 January 2022 are shown in Figure 2. The LOS Doppler
 157 velocities are scaled according to the color bar shown on the right. Negative velocities
 158 represent plasma flows moving away from the radar, while positive velocities represen-
 159 t plasma flows moving toward the radar. The slant range is the total distance traversed
 160 by the ray between the radar and the targets. The shadow in each panel indicates night.
 161 As shown in Figure 1, beam 0 of the JME radar points to the geographical North Pole,
 162 beam 4 of the HOK radar is almost parallel to beam 0 of the JME radar, and beam 4
 163 of the HKW and BKS radars points westward.

164 Before 0800 UT, backscatter with LOS velocities of less than ± 30 m/s was observed
 165 by beam 4 of the HOK radar and classified as ground backscatter. Distinct ionospheric
 166 backscatter began to be observed from 0800 UT on beam 4 of the HOK radar. Plas-
 167 ma with negative LOS velocities were observed first, with a minimum of approximat-
 168 ely -100 m/s, followed by a very short positive LOS velocity period with a maximum of
 169 approximately 60 m/s. Subsequently, a second sudden transition structure with a neg-

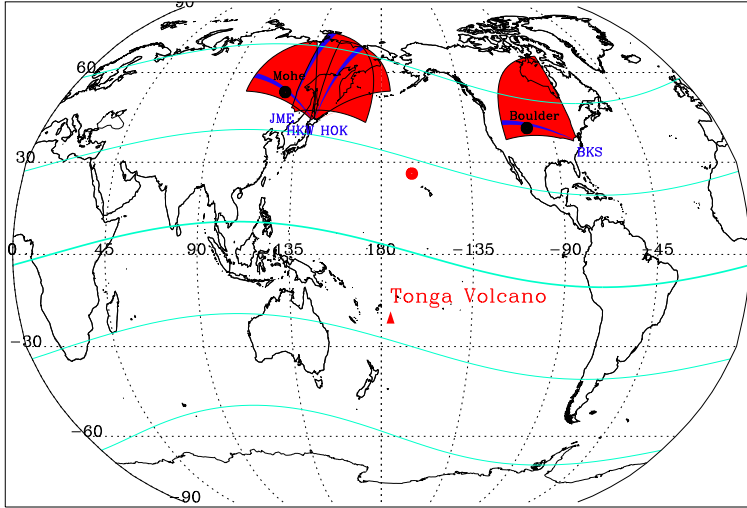


Figure 1. FOVs of the SuperDARN JME, HOK, HKW and BKS radars, where, beam 0 of the JME radar and beam 4 of the HOK, HKW and BKS radars are shaded in blue. The black dots represent the locations of the Mohe and Boulder digisondes. The red triangle indicates the location of the Tonga volcano, and the red dot indicates the magnetically conjugate point of the volcano. The cyan curves indicate the magnetic latitude lines with 30 degree intervals.

170 active LOS velocity was captured; this was followed by a short positive LOS velocity pe-
 171 riod, with velocity more rapid than the previous velocity. At 0900 UT, the third neg-
 172 ative velocity period, which lasted approximately one hour, with slower velocities than
 173 the second period, was observed. From 0800 UT and 1000 UT, the location of the echoes
 174 gradually moved to a further slant range. After 1000 UT, positive velocities were observed
 175 by the radars, and the location of the echoes gradually decreased to a closer slant range
 176 until 1130 UT. Beam 0 of the JME radar was approximately 1100 km west of beam 4
 177 of the HOK radar, and the two beams were nearly parallel to each other. Similar iono-
 178 spheric oscillation features with some time delay were observed from beam 4 of the HOK
 179 radar. As shown in Figure 2(b), from 0900 UT to 1200 UT, three negative/positive ve-
 180 locity periods, with a relatively short duration for the first two positive velocity periods
 181 (10 minutes), were observed by the JME radar. The second negative/positive veloc-
 182 ity period between 0920 UT and 1020 UT was the most rapid. The slant range of the
 183 observed echoes slowly increased from 0900 UT at approximately 500 km and rapidly
 184 dropped from a slant range of more than 1000 km at 1100 UT to a few hundred kilome-
 185 ters. Beam 4 of the HKW radar points westward. Figure 2 (c) shows that the observa-
 186 tions from beam 4 of the HKW radar are consistent with the observations from the HOK
 187 and JME radars. The positive LOS velocity regions moved to a farther slant range over
 188 time, indicating the westward propagation of the fluctuation.

189 Before 1120 UT, few backscatter in the slant range between 200 and 400 km (E lay-
 190 er of the ionosphere based on ray tracing simulations, please refer to Figure S1 in the
 191 supplemental material) were observed by beam 4 of the HOK radar. The magnitudes
 192 of the LOS velocities in this slant range were weaker than those in the slant range greater
 193 than 400 km (F layer of the ionosphere). According to data from surface pressure sta-
 194 tions, Wright et al. (2022) identified surface air pressure propagated as a Lamb wave at
 195 a phase speed of 318.2 ± 6 m/s. Shinbori et al. (2022) showed that the surface air pres-
 196 sure waves propagated to Japan at around 1120 UT as Lamb mode waves based on the
 197 thermal infrared grid data observed by the Himawari 8 satellite. After 1120 UT, much
 198 backscatter appeared in the E region of the ionosphere and were observed by the HOK

199 radar; the LOS velocities in the E layer exceeded ± 150 m/s and were stronger than those
 200 in the F region between 1120 UT and 1600 UT. After 1200 UT, the JME and HKW radars
 201 also observed an increase in the number of ionospheric echoes in the E layer.

202 According to the observations from the HOK and JME radars between 0800 UT
 203 and 1200 UT, the propagation direction of the ionospheric oscillation was westward. Af-
 204 ter the arrival of the surface air pressure waves, the propagation direction turned north-
 205 westward. Figure S2 in the supplemental material show the wavefronts observed by the
 206 HOK and JME radars at 0850 UT, 0940 UT and 1133 UT. The horizontal phase veloc-
 207 ity was approximately 330 m/s, which was calculated by using the delay time and the
 208 distance between the HOK radar and the JME radar. The propagation direction and
 209 horizontal phase velocity of the ionospheric fluctuations observed by the SuperDARN
 210 radars were consistent with the observations based on the TEC(Lin et al., 2022), which
 211 indicates that this group of oscillations was due to magnetic conjugate effect. Shinbori
 212 et al. (2022) also showed that the LOS Doppler velocity observed by the SuperDARN
 213 Hokkaido east radar was associated with the passage of TEC perturbations due to mag-
 214 netic conjugate effect. Strong ionospheric oscillations were observed by the SuperDARN
 215 radars in East Asia, with three LOS velocity transitions from 0800 UT to 1200 UT that
 216 may be attributed to the three main explosions of the volcanic eruptions in Tonga (Astafyeva
 217 et al., 2022; Wright et al., 2022). During this period, the slant range of the echoes showed
 218 a trend of rising, falling, and then rising, implying variations in the height of the iono-
 219 sphere in addition to oscillations in the horizontal direction.

220 The BKS radar is located in the Western Hemisphere and under different day-night
 221 conditions during the period of interest. The backscatter received by the BKS radar was
 222 considerably different from the backscatter received by the other three radars. Almost
 223 all of the backscatter was ground scatter. The velocity variation in ground scatter for
 224 the SuperDARN radars is usually attributed to vertical movement of the ionosphere. The
 225 BKS radar received minimal backscatter before 1200 UT as the radar operating frequen-
 226 cy and ionospheric conditions were not suitable. With sunrise, the ionosphere builds up
 227 and a band of ground scatter developed after 1230 UT. The slant range to the band varies
 228 and the LOS velocity fluctuates within narrow limits (< 30 m/s) throughout the day ow-
 229 ing to passage of TIDs, which is typical. However, after 1400 UT, ground scatter with
 230 LOS velocities greater than 90 m/s was observed by beam 4 of the BKS radar, corre-
 231 sponding to a marked downward motion in the ionosphere. Figure S3 in the supplemen-
 232 tal material shows the radar observations at 1440 UT, 1445 UT, and 1450 UT. This fig-
 233 ure clearly shows the downward motion of the ionosphere propagating northeastward.
 234 We estimated that the propagation velocity of the ionospheric fluctuation was approx-
 235 imately 320 m/s.

236 3.2 LOS velocity across different layers of ionosphere

237 To show the fluctuation velocity across different layers of the ionosphere, Figure
 238 3 shows an RTI plot of the LOS Doppler velocity observed by beam 4 of the HOK radar
 239 and line plots of the LOS velocities of range gates 2, 4, 10, 12, 14 and 16 for beam 4 of
 240 the HOK radar, with 10 min smoothing applied. The positive/negative velocities indi-
 241 cate that the direction of the LOS velocity was toward/away from the radar. Range gates
 242 2, 4, 10, 12, 14 and 16 correspond to slant ranges of 270, 360, 630, 720, 810 and 900 k-
 243 m, as indicated by the six black horizontal lines on Figure 3 (a). The blue vertical line
 244 at 0800 UT indicates the arrival time of the disturbance propagated from the magnet-
 245 ic conjugate point of the Tonga volcanic eruption, while the blue vertical line at 1120
 246 UT indicates the arrival time of the disturbance directly propagated from the Tonga vol-
 247 canic eruption. Between 0800 UT and 1120 UT, the maximum peak-to-peak amplitude
 248 of the ionospheric fluctuation velocity was approximately 150 m/s at range gate 10 (F
 249 layer) and was associated with the two shock structures. During this period, the peak-
 250 to-peak amplitude observed at gate 2 (E layer) was weaker than that observed in the F

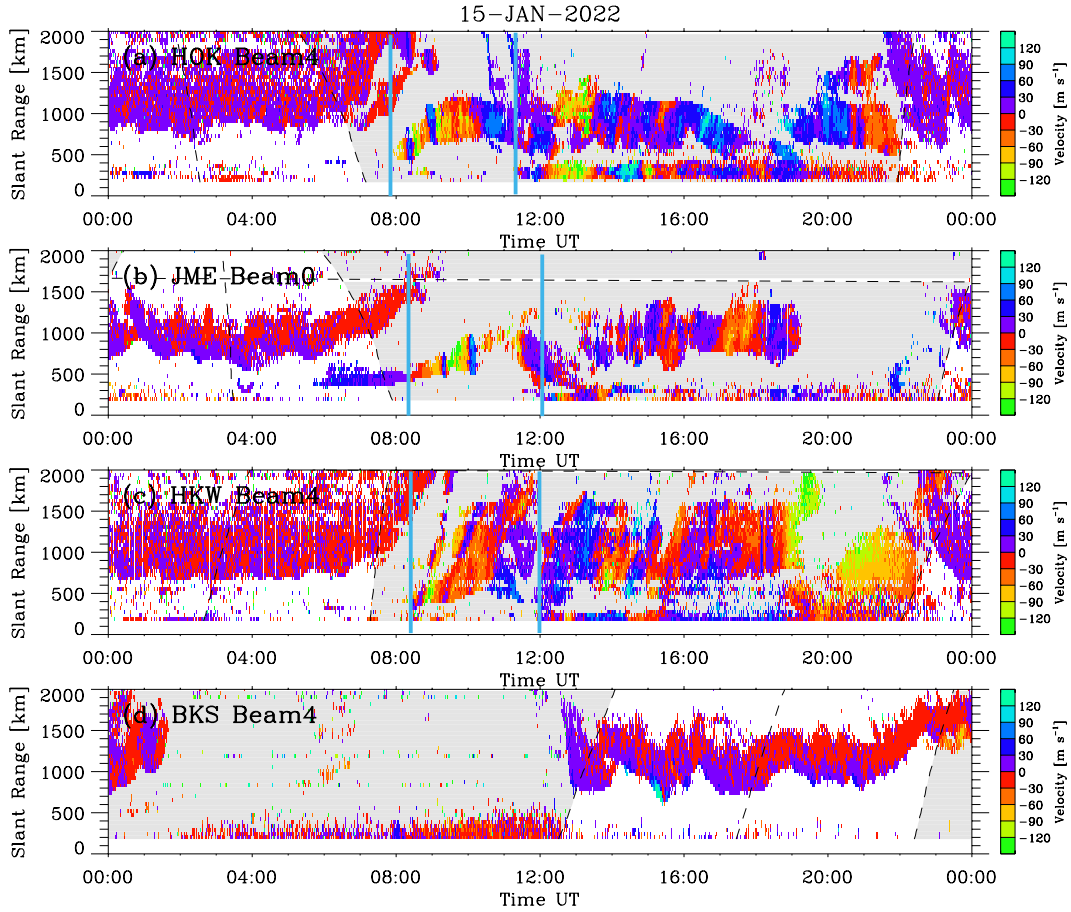


Figure 2. Range-time-intensity plots of the LOS Doppler velocities observed by (a) beam 4 of the HOK radar, (b) beam 0 of the JME radar, (c) beam 4 of the HKW radar and (d) beam 4 of the BKS radar on 15 January 2022. The LOS Doppler velocities are scaled according to the color bar shown on the right. The shadow in each panel indicates night. The two blue vertical lines in (a), (b) and (c) indicates the arrival time of the two groups of oscillations.

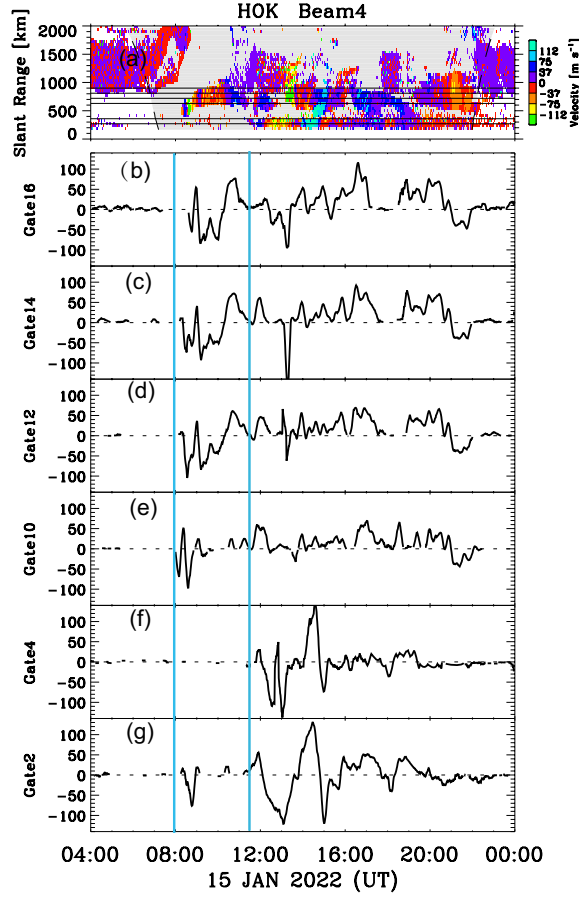


Figure 3. Fluctuation velocity across different layers of the ionosphere. (a) RTI plot of the LOS Doppler velocities observed by beam 4 of the HOK radar and line plots of the LOS velocities of range gates (b)16, (c) 14, (d) 12, (e) 10, (f) 4 and (g) 2 for beam 4 of the HOK radar, with 10 min smoothing applied. Range gates 2, 4, 10, 12, 14 and 16 correspond to slant ranges of 270, 360, 630, 720, 810 and 900 km, respectively, as indicated by the six black horizontal lines in Figure 4(a). The two vertical blue lines indicate the arrival time of the disturbance from the magnetic conjugate point of the volcanic eruption in Tonga and from the volcanic eruption itself.

251 layer. After the arrival of the surface air pressure waves at around 1120 UT, the maximum
 252 LOS velocity was approximately $\pm 150\text{m/s}$, and the peak-to-peak amplitude of the
 253 ionospheric fluctuation approached 300 m/s at range gate 4 (E layer). The peak-to-peak
 254 amplitude decreased over time and as the range gate increased.

255 **3.3 Uplift in the ionosphere by the volcanic eruption**

256 The SuperDARN radars observed the LOS velocity of the irregularities. To investigate
 257 the vertical motion of the ionosphere, we combined the observations from beam
 258 4 of the HKW radar and Mohe digisonde. Beam 4 of the HKW radar and the location
 259 of the Mohe digisonde are shown in Figure 1. Figure 4 shows the RTI plot of the LOS
 260 Doppler velocities observed by beam 4 of the HOK radar, the F layer peak height (h_mF_2)
 261 as a function of time obtained from the Mohe digisonde, and three representative
 262 ionograms to highlight the state of the ionosphere at specific times. The black horizontal
 263 dashed line in Figure 4 (a) indicates the radar slant range corresponding to the Mo-

264 he digisonde. The two vertical blue lines in Figure 4 (a) and (b) indicate the arrival time
 265 of the disturbance to the Mohe digisonde from the magnetic conjugate point of the vol-
 266 canic eruption in Tonga at 0930 UT and from the volcanic eruption itself at 1230 UT,
 267 respectively. The cyan dashed line in Figure 4 (b) indicates the variation in the peak height
 268 of the F layer during the quiet time (polynomial fitting curve based on observations on
 269 13 Jan 2022). As shown in Figure 4, the negative/positive LOS velocities of the HKW
 270 radar correspond to the upward/downward motion, respectively, of the ionosphere, which
 271 were captured by the Mohe digisonde, indicating that the LOS velocities observed by the
 272 SuperDARN radars have a pronounced vertical component and were not purely horizon-
 273 tal. After the arrival of the disturbance from the magnetic conjugate point of the vol-
 274 canic eruption at 0930 UT, an uplift of the ionosphere from 245 km to about 326 km was
 275 observed by the Mohe digisonde at 1030 UT, and then the height of the ionosphere vi-
 276 brated and fell to a normal height. After the disturbance from the volcanic eruption it-
 277 self propagated to Mohe at approximately 1230 UT, the uplift of the ionosphere was a-
 278 gain observed by the digisonde. Excluding the diurnal variation in the peak height of
 279 the F layer at the quiet time, the maximum amplitude of the vertical fluctuations caused
 280 by the volcanic eruption in Tonga was approximately 80 km, as observed by the Mohe
 281 digisonde. This finding indicates that the volcanic eruption caused strong vertical fluc-
 282 tuations of the ionosphere in the midlatitude region of the Northern Hemisphere. This
 283 vertical movement may be attributed to the fact that magnetic field lines in mid lati-
 284 tudes are not completely perpendicular to the ground; thus, east-west electric fields in
 285 this region will produce vertical movements of the ionosphere in addition to horizontal
 286 movements.

287 Joint observations from beam 4 of the BKS radar and Boulder digisonde also re-
 288 vealed the vertical oscillation of the ionosphere (see Figure S4 in the supplemental ma-
 289 terial). The position of the Boulder digisonde is beyond the 2000 km slant range of the
 290 BKS radar, so the location of the digisonde was not marked in the figure. A maximum
 291 positive velocity of approximately 90 m/s was observed by beam 4 of the BKS radar from
 292 1400 UT, which corresponds to a marked downward motion in the ionosphere. The Boul-
 293 der digisonde also observed the rapid decrease in the peak height of the F layer from 1400
 294 UT with an amplitude of more than 100 km, which is consistent with the observation
 295 from the BKS radar. The disturbance from the magnetic conjugate point of the volcanic
 296 eruption in Tonga and from the volcanic eruption itself arrived at the Boulder digisonde
 297 at 0905 UT and 1215 UT, respectively, which was calculated based on the speed of the
 298 Lamb wave.

299 4 Discussion and Conclusion

300 Figure S5 in the supplemental material shows the RTI plots of the LOS Doppler
 301 velocities observed by the four SuperDARN radars on 14 January 2022 and 15 January
 302 2022 with the SYM-H index. It was noted that there was a moderate storm during 14-
 303 15 January 2022, with the SYM-H index dropping to -101 nT at 2217 UT on 14 January
 304 2022. Analyses by Lin et al. (2022) and Shinbori et al. (2022) showed that the IMF Bz
 305 turned northward at 2330 UT on 14 January 2022, and the AE index remained at a very
 306 low level from 0400 UT to 1100 UT on 15 January 2022. When the eruption occurred,
 307 the storm was in the late recovery phase. Geomagnetic storms are known to generate
 308 LSTIDs that propagate from high latitudes to equatorward (e.g., Richmond, 1978, and
 309 others). The perturbations propagated westward and northwestward in East Asia and
 310 propagated northeastward in the United States. The propagation direction and veloc-
 311 ity were different from the propagation feature of the storm-time LSTIDs, and they were
 312 consistent with the features of the TIDs caused by the volcanic eruption.

313 According to the observations from the SuperDARN radars in East Asia, the strongest
 314 LOS velocity appeared in the F layer of the ionosphere due to the magnetic field con-
 315 jugate effect, and the amplitude of the velocity decreased with decreasing altitude. This

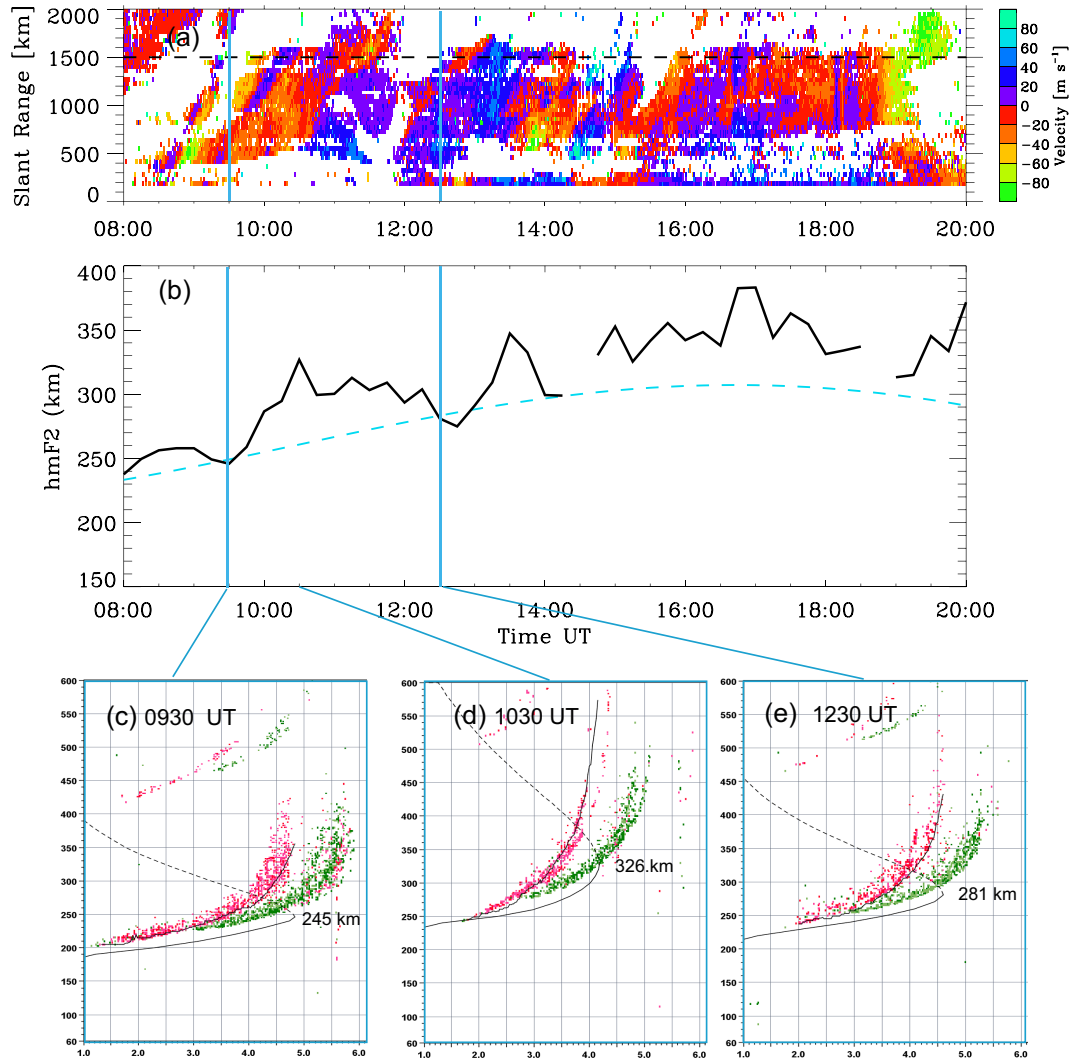


Figure 4. Vertical variation of the ionosphere. (a) RTI plot of the LOS Doppler velocities observed by beam 4 of the HOK radar. The black horizontal dashed line in panel (a) indicates the slant range corresponding to the Mohe digisonde. (b) Ionospheric peak height of the F2 layer as a function of time obtained from the Mohe digisonde. The two vertical blue lines in panel (a) and (b) indicate the arrival time of the disturbance to the Mohe digisonde from the magnetic conjugate point of the volcanic eruption in Tonga and from the volcanic eruption itself, respectively. The cyan dashed curve in panel (b) indicates the variation in the peak height of the F layer of the ionosphere during the quiet time. Three representative ionograms are shown at (c) 0930 UT, (d) 1045 UT and (e) 1230 UT.

316 finding indicates that the magnetic field conjugate effect has a significant impact on the
317 plasma flow in the F layer in another hemisphere. During this period, the ionospheric
318 plasma flow was produced by an external electric field that was generated by an E lay-
319 er dynamo in the sunlit Southern Hemisphere. The two sudden increases of the plasma
320 flow may correspond to the two large Tonga eruptions with VEI values of 6, which can
321 cause a significant enhancement of an E-region dynamo electric field. After the arrival
322 of surface air pressure waves, the strongest LOS velocity appeared in the E layer, and
323 the amplitude of the velocity decreased with increasing altitude. During this period, the
324 ionospheric conductivity of the E-region was very small due to the dark region, and the
325 E layer dynamo process was not effective on the ionospheric plasma motion in the F-region.
326 Thus, the E and F layer motions were directly produced by the neutral wind oscillation
327 associated with arrival of the air pressure waves. The collision frequency was much s-
328 maller in the F layer than in the E layer. Therefore, the plasma motion was expected
329 to be slower in the F layer than in the E layer.

330 The fluctuation caused by the magnetic field conjugate effect was detected by three
331 radars in East Asia, while the BKS radar in America did not record fluctuations caused
332 by the magnetic field conjugate effect. This was attributed to the fact that the radar op-
333 erating frequency and ionospheric conditions did not satisfy the conditions for receiving iono-
334 spheric backscatter during the relevant period. In addition, the three midlatitude Su-
335 perDARN radars in Australia and New Zealand in the Southern Hemisphere were not
336 operating during this period. If these radars were operational, they would have provid-
337 ed excellent observations for comparing movements in the ionosphere caused by volcanic
338 eruptions in the Southern and Northern Hemispheres, and would have contributed to a
339 deeper understanding of the mechanisms underlying the magnetic field conjugate effec-
340 t.

341 In conclusion, impacts on ionospheric irregularities and ionospheric oscillation fea-
342 tures in the Northern Hemisphere caused by the explosive Tonga volcanic eruption in
343 the southwest Pacific were clearly captured by midlatitude SuperDARN radars and digison-
344 des. The ionospheric fluctuations observed by SuperDARN radars in East Asia propa-
345 gated westward due to the magnetic field conjugate effect. After the surface pressure waves
346 arrived, the propagation direction was northwestward. The distant and upward motion-
347 s of the ionosphere was considerably more rapid and lasted longer than the forward and
348 downward motions. Because of different mechanisms, the maximum peak-to-peak LOS
349 velocity of the ionosphere exceeded 150 m/s appeared in F layer due to the magnetic field
350 conjugate effect, and the maximum peak-to-peak LOS velocity of the ionosphere was ap-
351 proximately 300 m/s and appeared in the E layer due to the direct propagation of the
352 wave from the Tonga volcano. The amplitude of the vertical rise and fall of the ionosphere
353 in the mid-latitude region of the Northern Hemisphere reached nearly 100 km due to the
354 volcanic eruption. This event shows how geological hazards can impact the ionosphere
355 and cause space weather, raising concerns for vulnerable technologies.

356 5 Open Research

357 The raw SuperDARN data are available from the SuperDARN data server at the
358 National Space Science Center, Chinese Academy of Sciences (<https://superdarn.nssdc.ac.cn/>).
359 To access the data, users should log in, and go to ‘Access data’ to select the radar, dataset
360 and date. The Mohe ionogram data were obtained from the Chinese Meridian Project
361 Database (<https://data.meridianproject.ac.cn/>), to access the data, users also should log
362 in, and go to ‘Download’, then select ‘Mohe station’, and then choose ‘Ionogram image
363 of digital ionosonde’. The Boulder ionogram data were obtained from the Digital Iono-
364 gram Database (<http://spase.info/SMWG/Observatory/GIRO>). The SYM-H index can
365 be downloaded from World Data Center for Geomagnetism, Kyoto ([doi:10.14989/267216](https://doi.org/10.14989/267216)).

Acknowledgments

This work was supported by NNSFC grants 41731070, 42174210, and 42188101. This work was also supported by the Key Research Program of Frontier Sciences CAS Grant No. QYZDJ-SSW-JSC028 and the Specialized Research Fund for the State Key Laboratories of China. We also acknowledge the Chinese Meridian Project.

References

- Adam, D. (2022). Tonga volcano eruption created puzzling ripples in earths atmosphere [Journal Article]. *Nature*, *602*, 497. doi: <https://doi.org/10.1038/d41586-022-00127-1>
- Astafyeva, E., Maletckii, B., Mikesell, T. D., Munaibari, E., Ravanelli, M., Coisson, P., ... Rolland, L. (2022). The 15 january 2022 hunga tonga eruption history as inferred from ionospheric observations [Journal Article]. *Geophysical Research Letters*, *49*(10), e2022GL098827. Retrieved from <https://agupubs.onlinelibrary.wiley.com/doi/abs/10.1029/2022GL098827> doi: <https://doi.org/10.1029/2022GL098827>
- Carr, J. L., Horvth, k., Wu, D. L., & Friberg, M. D. (2022). Stereo plume height and motion retrievals for the record-setting hunga tonga-hunga ha'apai eruption of 15 january 2022 [Journal Article]. *Geophysical Research Letters*, *49*(9), e2022GL098131. Retrieved from <https://agupubs.onlinelibrary.wiley.com/doi/abs/10.1029/2022GL098131> doi: <https://doi.org/10.1029/2022GL098131>
- Chisham, G., Lester, M., Milan, S. E., Freeman, M., Bristow, W., Grocott, A., ... Dyson, P. L. (2007). A decade of the super dual auroral radar network (superdarn): Scientific achievements, new techniques and future directions [Journal Article]. *Surveys in geophysics*, *28*(1), 33-109.
- Dautermann, T., Calais, E., & Mattioli, G. S. (2009). Global positioning system detection and energy estimation of the ionospheric wave caused by the 13 July 2003 explosion of the soufriere hills volcano, montserrat [Journal Article]. *Journal of Geophysical Research: Solid Earth*, *114*(B2). Retrieved from <https://agupubs.onlinelibrary.wiley.com/doi/abs/10.1029/2008JB005722> doi: <https://doi.org/10.1029/2008JB005722>
- Greenwald, R. A., Baker, K. B., Dudeney, J. R., Pinnock, M., Jones, T. B., Thomas, E. C., ... Yamagishi, H. (1995). Darn/superdarn [Journal Article]. *Space Science Reviews*, *71*(1), 761-796. Retrieved from <https://doi.org/10.1007/BF00751350> doi: 10.1007/BF00751350
- Heki, K. (2006). Explosion energy of the 2004 eruption of the asama volcano, central japan, inferred from ionospheric disturbances [Journal Article]. *Geophysical Research Letters*, *33*(14). Retrieved from <https://agupubs.onlinelibrary.wiley.com/doi/abs/10.1029/2006GL026249> doi: <https://doi.org/10.1029/2006GL026249>
- Huang, C. Y., Helmboldt, J. F., Park, J., Pedersen, T. R., & Willemann, R. (2019). Ionospheric detection of explosive events [Journal Article]. *Reviews of Geophysics*, *57*(1), 78-105. Retrieved from <https://agupubs.onlinelibrary.wiley.com/doi/abs/10.1029/2017RG000594> doi: <https://doi.org/10.1029/2017RG000594>
- Lin, J.-T., Rajesh, P. K., Lin, C. C. H., Chou, M.-Y., Liu, J.-Y., Yue, J., ... Kung, M.-M. (2022). Rapid conjugate appearance of the giant ionospheric lamb wave signatures in the northern hemisphere after hunga-tonga volcano eruptions [Journal Article]. *Geophysical Research Letters*, *49*(8), e2022GL098222. Retrieved from <https://agupubs.onlinelibrary.wiley.com/doi/abs/10.1029/2022GL098222> doi: <https://doi.org/10.1029/2022GL098222>
- Liu, C. H., Klostermeyer, J., Yeh, K. C., Jones, T. B., Robinson, T., Holt, O., ... Kersley, L. (1982). Global dynamic responses of the atmosphere to the eruption

- 419 of mount st. helens on may 18, 1980 [Journal Article]. *Journal of Geophys-*
 420 *ical Research: Space Physics*, 87(A8), 6281-6290. Retrieved from [https://](https://agupubs.onlinelibrary.wiley.com/doi/abs/10.1029/JA087iA08p06281)
 421 agupubs.onlinelibrary.wiley.com/doi/abs/10.1029/JA087iA08p06281
 422 doi: <https://doi.org/10.1029/JA087iA08p06281>
- 423 Liu, X., Xu, J., Yue, J., & Kogure, M. (2022). Strong gravity waves associated with
 424 tonga volcano eruption revealed by saber observations [Journal Article]. *Geo-*
 425 *physical Research Letters*, 49(10), e2022GL098339. Retrieved from [https://](https://agupubs.onlinelibrary.wiley.com/doi/abs/10.1029/2022GL098339)
 426 agupubs.onlinelibrary.wiley.com/doi/abs/10.1029/2022GL098339 doi:
 427 <https://doi.org/10.1029/2022GL098339>
- 428 Meng, X., Vergados, P., Komjathy, A., & Verkhoglyadova, O. (2019). Upper at-
 429 mospheric responses to surface disturbances: An observational perspective
 430 [Journal Article]. *Radio Science*, 54(11), 1076-1098. Retrieved from [https://](https://agupubs.onlinelibrary.wiley.com/doi/abs/10.1029/2019RS006858)
 431 agupubs.onlinelibrary.wiley.com/doi/abs/10.1029/2019RS006858 doi:
 432 <https://doi.org/10.1029/2019RS006858>
- 433 Nishitani, N., Ogawa, T., Otsuka, Y., Hosokawa, K., & Hori, T. (2011). Propagation
 434 of large amplitude ionospheric disturbances with velocity dispersion observed
 435 by the superdarn hokkaido radar after the 2011 off the pacific coast of tohoku
 436 earthquake [Journal Article]. *Earth Planets and Space*, 63(7), 891-896.
- 437 Nishitani, N., Ruohoniemi, J. M., Lester, M., Baker, J. B. H., Koustov, A. V.,
 438 Shepherd, S. G., ... Kikuchi, T. (2019). Review of the accomplish-
 439 ments of mid-latitude super dual auroral radar network (superdarn) hf
 440 radars [Journal Article]. *Progress in Earth and Planetary Science*, 6(1),
 441 27. Retrieved from <https://doi.org/10.1186/s40645-019-0270-5> doi:
 442 [10.1186/s40645-019-0270-5](https://doi.org/10.1186/s40645-019-0270-5)
- 443 Poli, P., & Shapiro, N. M. (2022). Rapid characterization of large volcanic eruptions:
 444 Measuring the impulse of the hunga tonga haapai explosion from teleseismic
 445 waves [Journal Article]. *Geophysical Research Letters*, 49(8), e2022GL098123.
 446 Retrieved from [https://agupubs.onlinelibrary.wiley.com/doi/abs/](https://agupubs.onlinelibrary.wiley.com/doi/abs/10.1029/2022GL098123)
 447 [10.1029/2022GL098123](https://agupubs.onlinelibrary.wiley.com/doi/abs/10.1029/2022GL098123) doi: <https://doi.org/10.1029/2022GL098123>
- 448 Reinisch, B. W., & Galkin, I. A. (2011). Global ionospheric radio observatory (giro).
 449 *Earth, Planets and Space*, 63(4), 377-381. doi: 10.5047/eps.2011.03.001
- 450 Ribeiro, A., Ruohoniemi, J., Ponomarenko, P., N Clausen, L., H Baker, J., Green-
 451 wald, R., ... Larquier, S. (2013). A comparison of superdarn acf fitting
 452 methods [Journal Article]. *Radio Science*.
- 453 Richmond, A. D. (1978). Gravity wave generation, propagation, and dissipa-
 454 tion in the thermosphere [Journal Article]. *Journal of Geophysical Re-*
 455 *search: Space Physics*, 83(A9), 4131-4145. Retrieved from [https://](https://agupubs.onlinelibrary.wiley.com/doi/abs/10.1029/JA083iA09p04131)
 456 agupubs.onlinelibrary.wiley.com/doi/abs/10.1029/JA083iA09p04131
 457 doi: <https://doi.org/10.1029/JA083iA09p04131>
- 458 Roberts, D. H., Klobuchar, J. A., Fougere, P. F., & Hendrickson, D. H. (1982). A
 459 large-amplitude traveling ionospheric disturbance produced by the may 18,
 460 1980, explosion of mount st. helens [Journal Article]. *Journal of Geophys-*
 461 *ical Research: Space Physics*, 87(A8), 6291-6301. Retrieved from [https://](https://agupubs.onlinelibrary.wiley.com/doi/abs/10.1029/JA087iA08p06291)
 462 agupubs.onlinelibrary.wiley.com/doi/abs/10.1029/JA087iA08p06291
 463 doi: <https://doi.org/10.1029/JA087iA08p06291>
- 464 Shinbori, A., Otsuka, Y., Sori, T., Nishioka, M., Perwitasari, S., Tsuda, T., & Nishi-
 465 tani, N. (2022). Electromagnetic conjugacy of ionospheric disturbances after
 466 the 2022 hunga tonga-hunga haapai volcanic eruption as seen in gnss-tec and
 467 superdarn hokkaido pair of radars observations [Journal Article]. *Earth,*
 468 *Planets and Space*, 74(1), 106. Retrieved from [https://doi.org/10.1186/](https://doi.org/10.1186/s40623-022-01665-8)
 469 [s40623-022-01665-8](https://doi.org/10.1186/s40623-022-01665-8) doi: 10.1186/s40623-022-01665-8
- 470 Themens, D. R., Watson, C., ?agar, N., Vasylyevych, S., Elvidge, S., McCaffrey, A.,
 471 ... Jayachandran, P. T. (2022). Global propagation of ionospheric distur-
 472 bances associated with the 2022 tonga volcanic eruption [Journal Article]. *Geo-*
 473 *physical Research Letters*, 49(7), e2022GL098158. Retrieved from <https://>

- 474 agupubs.onlinelibrary.wiley.com/doi/abs/10.1029/2022GL098158 doi:
475 <https://doi.org/10.1029/2022GL098158>
476 Wright, C. J., Hindley, N. P., Alexander, M. J., Barlow, M., Hoffmann, L.,
477 Mitchell, C. N., ... Yue, J. (2022). Surface-to-space atmospheric waves
478 from hunga tonga-hunga haapai eruption [Journal Article]. *Nature*. Re-
479 trieved from <https://doi.org/10.1038/s41586-022-05012-5> doi:
480 [10.1038/s41586-022-05012-5](https://doi.org/10.1038/s41586-022-05012-5)
481 Zhang, S.-R., Vierinen, J., Aa, E., Goncharenko, L. P., Erickson, P. J., Rideout, W.,
482 ... Spicher, A. (2022). 2022 tonga volcanic eruption induced global propaga-
483 tion of ionospheric disturbances via lamb waves [Journal Article]. *Frontiers in*
484 *Astronomy and Space Sciences*, 9. doi: [10.3389/fspas.2022.871275](https://doi.org/10.3389/fspas.2022.871275)